Journal of Alloys and Compounds 969 (2023) 172279

Contents lists available at ScienceDirect

Journal of Alloys and Compounds

journal homepage: www.elsevier.com/locate/jalcom

High temperature shock synthesis of superfine Ru nanoparticles anchored on TiO_2 @nitrogen-doped carbon for pH-universal hydrogen evolution reaction

Jinxiu Cai [a], Lingbo Zong [a,*], Kaicai Fan [b], Fuxiang Song [a], Jianyang Gao [c], Zumin Wang [d,*], Yanan Chen [e], Lei Wang [a,*]

[a] Key Laboratory of Eco-chemical Engineering, College of Chemistry and Molecular Engineering, Qingdao University of Science and Technology, Qingdao 266042, China
[b] College of Materials Science and Engineering, Qingdao University of Science and Technology, Qingdao 266042, China
[c] College of Chemical Engineering, Qingdao University of Science and Technology, Qingdao 266042, China
[d] State Key Laboratory of Biochemical Engineering, Institute of Process Engineering, Chinese Academy of Sciences, 1 North 2nd Street, Zhongguancun, Haidian District, Beijing 100190, China
[e] School of Materials Science and Engineering, Tianjin University, Tianjin 300072, China

ARTICLE INFO

Keywords:
High temperature thermal shock
Ru nanoparticle
Hydrogen evolution reaction
pH-universal

ABSTRACT

Due to energy crisis and environmental pollution, it is urgent to develop efficient and cheap catalysts for hydrogen production from water electrolysis. As a cheaper platinum group metal, Ru, a cheaper platinum group metal, is a highly competitive candidate to Pt because of the similar bond energy of M-H. Herein, TiO_2 @nitrogen-doped carbon composite supported superfine Ru nanoparticles was synthesized by high temperature shock in a Joule furnace using Ti-MOF support (Ru/TiO_2 @NC-J). In the extremely rapid process, MOF was quickly converted into highly conductive nitrogen-doped carbon with tiny TiO_2 dispersed in it, and superfine Ru nanoparticles were generated simultaneously in less than 0.5 s. The obtained Ru/TiO_2 @NC-J displays wonderful HER performance in the wide pH range. In 1.0 M KOH solution, the overpotential was as low as 11 mV at 10 mA cm^{-2} and a Tafel slope was 39.2 mV dec^{-1}, which far exceeded the activity of Pt/C and conventional calcined samples as well as most of the recently reported catalysts. The as-developed electrocatalysts also showed excellent stability to accommodate large working current for long term test without obvious activity loss in universal pH range. Experimental investigations suggest that the strong metal-support interaction dominantly facilitate the activity of electrocatalytic hydrogen evolution reaction (HER), and stability of Ru/TiO_2 @NC-J. This strategy provides a new and super-fast methodology to prepare low-budget and high-performance HER catalysts for practical applications.

1. Introduction

With the increasing environmental pollution and the depleting of fossil fuels, the need for clean energy and renewable energy becomes more and more urgent [1]. Hydrogen energy is well-accepted as a promising new generation fuel because of its abundant reserves, high energy density and pollution-free [2–6]. Water electrolysis driven by from renewable energy is an important technology to produce hydrogen. However, electrochemical water splitting is restricted by the slow hydrogen evolution reaction (HER) kinetics [7,8]. In order to boost the production of hydrogen, stable and efficient electrocatalysts are needed. In the industry, platinum (Pt)-based materials are the most commonly used HER electrocatalysts, which have extremely high current density and reaction kinetics. Unfortunately, they are scarce and expensive for large industrial application. Therefore, it is of significant urgency to design low price, high efficiency and high stability electrocatalysts to replace Pt [9].

Materials scientists have been considering nonprecious metal compound catalysts as alternative options, such as transitional metal oxides [10,11], sulfides [12], nitrides [13,14], selenides [15,16] and phosphide [17,18]. Doping or alloying non-noble hetero elements with host catalysts have been widely used s to explore new alternatives to Pt [19,20]. For example, doping of 3d transition metals such as Fe, Co, and Ni have been proven effective to improve HER activity [21,22]. Unfortunately,

* Corresponding authors.
E-mail addresses: lingbozong@qust.edu.cn (L. Zong), wangzm@ipe.ac.cn (Z. Wang), inorchemwl@126.com (L. Wang).

https://doi.org/10.1016/j.jallcom.2023.172279
Received 23 June 2023; Received in revised form 27 August 2023; Accepted 20 September 2023
Available online 23 September 2023

those materials are usually limited by low efficiency and instability because of their susceptibility to corrosion in strong acid or basic solution [23]. Moreover, their performances are still far from approaching those of precious metal-based catalysts [24,25]. So, although over the last several decades have witnessed the prosperity of noble metal-free electrocatalysts with encouraging catalytic performance, few of them have comparable HER activity and stability with benchmark Pt-based electrocatalysts [26,27].

Ruthenium (Ru), one of the cheapest noble metals, shows great potentials to be alternative HER electrocatalysts because it has only 4% of the cost of Pt but similar electron configuration like Pt [28–30]. So, Ru has moderate H* adsorption energy, strong anticorrosive ability and excellent activity in a wide pH range [31,32]. Moreover, Ru has stronger oxyphilic binding, leading to better water dissociation ability [33]. Thus, previous reports have revealed that some Ru-based catalysts show comparable intrinsic HER activity or even better than that of Pt, especially in neutral or alkaline solution [34,35]. However, because of their high surface energy, Ru nanoparticles prone to aggregate, which leads to the degradation of HER performance. Therefore, evenly dispersing or anchoring Ru nanoparticles on suitable support with large specific area becomes a feasible strategy, which can not only reduce the usage of noble metals, but also improve the catalytic performance of the catalyst [7,36].

Metal-organic framework (MOF) is a class of crystalline porous materials composed of different metal nodes and organic linkers [37]. Being versatile and tailorable, MOF has excellent chemical adjustability and controlled function without changing the structure, which allows us to flexibly design the materials. Notably, materials (oxide [38], carbon [39] etc.) derived from MOFs have higher porosity and larger surface area, which can enhance mass transfer and diffusion during the reaction process [40]. The carbon components produced through direct pyrolysis of organic ligands can also promote electron transfer throughout the structure. At the same time, carbon components can effectively anchor nanoparticles, ensuring their small size and high dispersion, and improving the final catalytic activity [41]. Therefore, MOF shows great advantages in the construction of efficient electrocatalysts with desired compositions and dispersion states [42–44].

Joule heating strategy, which possesses flash heating and cooling process, has been reported as a facile method to load nanoparticles on carbon support [45]. The operating principle of the Joule thermal fast synthesizer is that high temperature shock can be realized in the process of synthesis of transient heating and quenching process of electrical pulses [46]. In this work, we used Joule heating method to rapidly calcinate the MOF material at 1500 ℃ within 0.5 s. Within very limited time, the high temperature made the MOF discomposed and carbonized, giving rise to tiny TiO_2 crystals that were dispersed within nitrogen doped carbon (NC). At the same time, the ultra-small sized Ru nanoparticles were simultaneously formed and uniformly fixed on the support, forming a new supported catalyst noted as Ru/TiO_2 @NC-J. Because of the uniform loading of ultrafine Ru nanoparticles on the large surface area support, abundant active sites are exposed. At the same time, Strong Metal-Support Interaction (SMSI) creates, which promotes electron transfer and thus increases the electrocatalytic HER activity. As the result, the overpotential of Ru/TiO_2 @NC-J at a current density of 10 mA cm^{-2} in 1.0 M KOH alkaline electrolyte was as low as 11 mV, and the Tafel slop was only 39.2 mV dec^{-1}, which was superior to commercially available Pt/C (20 wt%). The as-prepared electrocatalyst also showed excellent activity as well as superior durability in acid and neutral media. The present result demonstrates a rapid and convenient way to prepare cheap and efficient electrocatalysts.

2. Experimental sections

2.1. Materials and chemicals

Tetrabutyl titanate ($Ti(OCH_2CH_2CH_2CH_3)_4$, 97%), 2-aminoterephthalic acid ($H_2BDC\text{-}NH_2$, 99%), $RuCl_3$ were obtained from Sigma Aldrich. Nafion 117 solution (~5%), Pt/C (20 wt%) were obtained from Aladdin Reagent Technology Co., Ltd. Methanol, ethanol, NaOH (analytical grade), KOH (analytical grade), and N, N-Dimethylformamide (DMF, 99.9%) were obtained from the Sinopharm Chemical Reagent Co., Ltd. All the reagents were used as received without any further purification.

2.2. Synthesis of Ti-MOF

Ti-MOF were synthesized via developed hydrothermal method [47]. DMF (7.5 mL), methanol (2.5 mL) and 2-aminoterephthalic acid (0.21 g) were added to a 30 mL hydrothermal kettle, stirred and evenly dissolved, then 0.225 mL tetrabutyl titanate was added and continued to stir for 5 min. Then, the above solution was put into autoclave and heated at 150 ℃ for 12 h. The precipitate was collected, washed and dried in a vacuum drying oven at 60 ℃ overnight to obtain yellow powder.

2.3. Synthesis of TiO_2 @NC-J

The precursor, Ti-MOF, were then obtained after collecting, washing and drying. Put the powder into a vacuum drying oven and dried overnight at 60 ℃ to obtain yellow powder. Finally, the sample was calcined 0.5 s in a Joule oven at 1500 ℃ under nitrogen atmosphere.

2.4. Synthesis of Ru/TiO_2 @NC-J

The 100 mg Ti-MOF powder was dissolved in 20 mL deionized water and then ultrasonically dispersed for 5 min. Afterwards, 10 mL of 2 mg/mL of $RuCl_3$ solution was added to the mixture, followed by further ultrasonic treatment for 40 min, stirred for 24 h. After collecting, washing and drying, put the thoroughly mixed powder (Ru^{3+}/Ti-MOF) into a vacuum drying oven and dried overnight at 60 ℃ to obtain yellow powder. Finally, the sample was calcined 0.5 s in a Joule oven at 1500 ℃ under nitrogen atmosphere.

2.5. Synthesis of Ru/TiO_2 @NC-T

The 100 mg Ti-MOF powder was dissolved in 20 mL deionized water and then ultrasonically dispersed for 5 min. Then 10 mL of 2 mg/mL of $RuCl_3$ water solution was added to the mixture, followed by further ultrasonic treatment for 40 min, stirred for 24 h. After collecting, washing and drying, put the thoroughly mixed powder (Ru^{3+}/Ti-MOF) into a vacuum drying oven and dried overnight at 60 ℃ to obtain yellow powder. Finally, the sample was calcined in a tube oven at a rate of 2 degrees per minute to 800 ℃ for 3 h under nitrogen atmosphere to get the Ru/TiO_2 @NC-T.

3. Results and discussion

3.1. Preparation and characterization

Fig. 1 schematically depicts the synthesis procedure of Ru/TiO_2 @NC-J. Briefly, Ti-MOF was firstly synthesized by hydrothermal reaction of 2-amino-terephthalic acid ($H_2BDC\text{-}NH_2$) and tetra-butyl titanate ($C_{16}H_{36}O_4Ti$) [47]. Secondly, with Ti-MOF as the substrate, a certain amount of $RuCl_3$ was introduced through adsorption. Especially for amine-functionalized MOFs, the free amine groups (-NH_2) efficiently stabilized metal cations via strong coordination between its lone pair electrons and empty d-orbitals of transition metal atom [48], therefore, more Ru^{3+} ions were anchored by NH_2 groups. After a rapid shock in the Joule furnace at 1500 ℃ under N_2 atmosphere, Ru species quickly reduced into metallic form. And Ti-MOF was transformed into composite that were mainly composed by TiO_2 and nitrogen doped carbon (NC). Moreover, because of the high temperature shock, the temperature

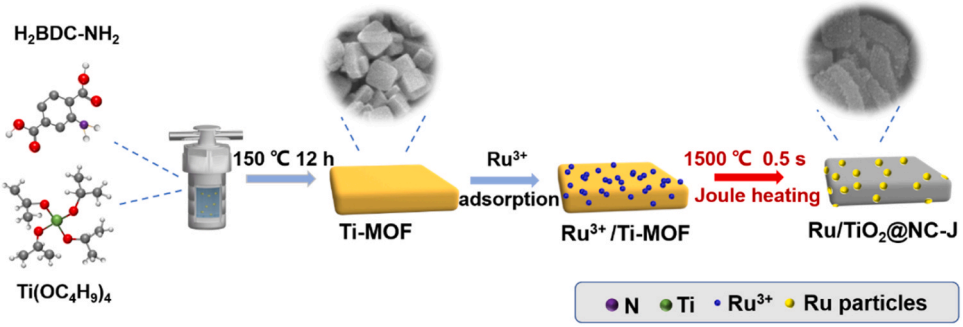

Fig. 1. Schematic illustration of the synthesis of Ru/TiO_2 @NC-J.

raised and dropped too quickly for the atoms to migrate and aggregate, which leaded to even and uniform dispersion of very tiny nanoparticles [49]. From the scanning electron microscopy (SEM) images, X-ray diffraction (XRD) pattern and Fourier transform infrared (FTIR) spectra in Fig. S1, Fig. S2, and Fig. S3, it was clear that the synthesized Ti-MOF had a well-defined three-dimensional block structure.

After a rapid thermal shock, the obtained Ru/TiO_2 @NC-J demonstrated a morphology of the similar size and shape but with a much rougher surface, indicating the successful loading of Ru particles (Fig. 2a). In Fig. 2b, transmission electron microscopy (TEM) also showed that the Ti-MOF substrate retained the original morphology after calcination but with some darker spots, which was believed to be Ru particles. The selective area electron diffraction (SAED) pattern also demonstrated the clearly ring of Ru and TiO_2 species (Fig. 2b inset), which agreed with the HRTEM results (Fig. 2c). From more detailed observation, it was clear that the size of TiO_2 particle was about 20 nm and the size of Ru particle was about 3.5 nm (the inset of Fig. 2c). However, the size of Ru in catalyst Ru/TiO_2 @NC-T obtained by ordinary calcination method is mostly 5.5 nm (Fig. S4). With this extremely fast calcination process, the size of ultrafine Ru particles in Ru/TiO_2 @NC-T obtained by high-temperature shock is smaller, so the catalyst has more active sites and has a larger active surface area. The lattice spacing of 0.32 nm in the high-resolution transmission electron microscope (HRTEM) image can be attributed to the (110) crystal plane of the rutile phase TiO_2. The lattice spacing of 0.21 nm, corresponded to the hexagonal Ru (002) plane (Fig. 2c). Moreover, the TEM-EDS (Fig. 2d) showed the uniform spatial distribution of C, N, O, Ti and Ru elements in Ru/TiO_2 @NC-J, suggesting the uniform dispersion of ultrafine Ru nanoparticles on the support.

The XRD pattern (Fig. 3a) further testified that the generated Ru

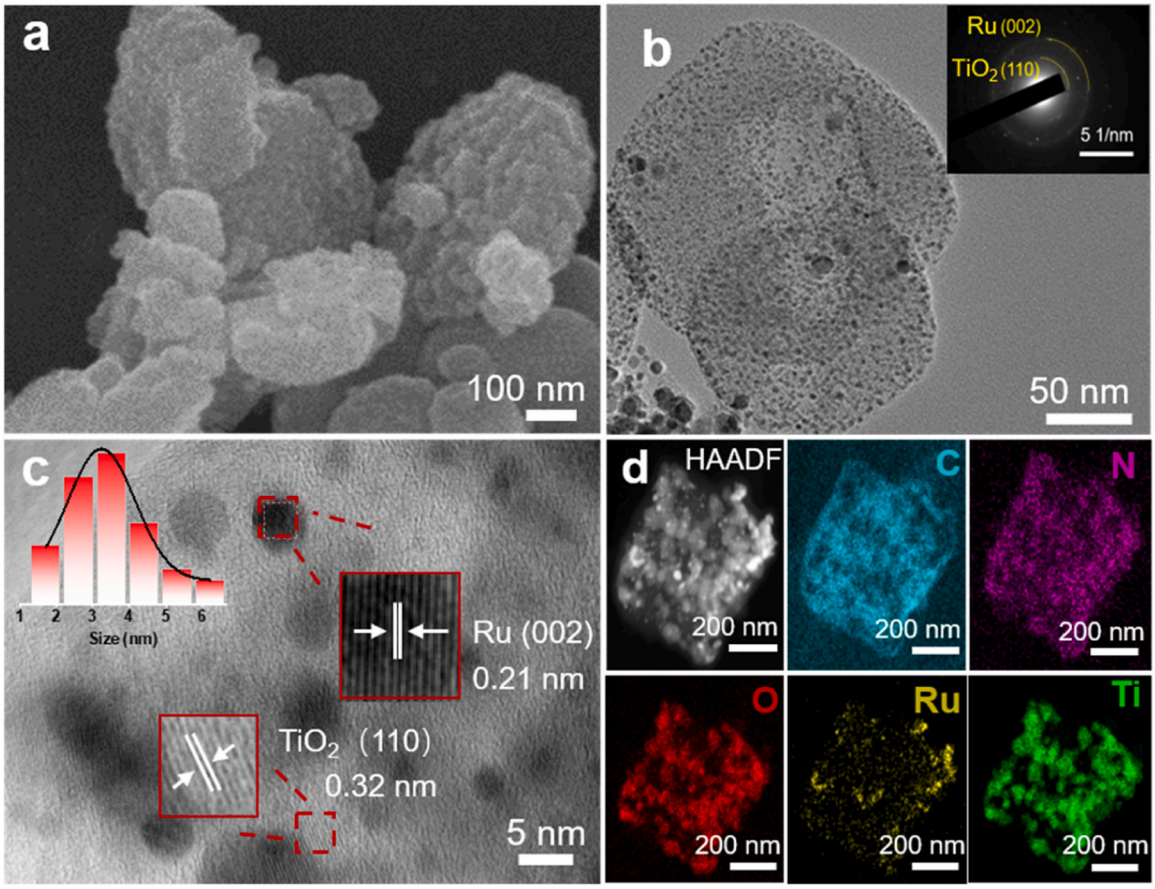

Fig. 2. (a) SEM image of Ru/TiO_2 @NC-J. (b) TEM image of Ru/TiO_2 @NC-J. Inset: the corresponding SAED patterns. (c) HRTEM image of Ru/TiO_2 @NC-J. Inset: the corresponding size distribution of Ru. (d) HAADF-STEM images and corresponding EDX maps of Ru/TiO_2 @NC-J.

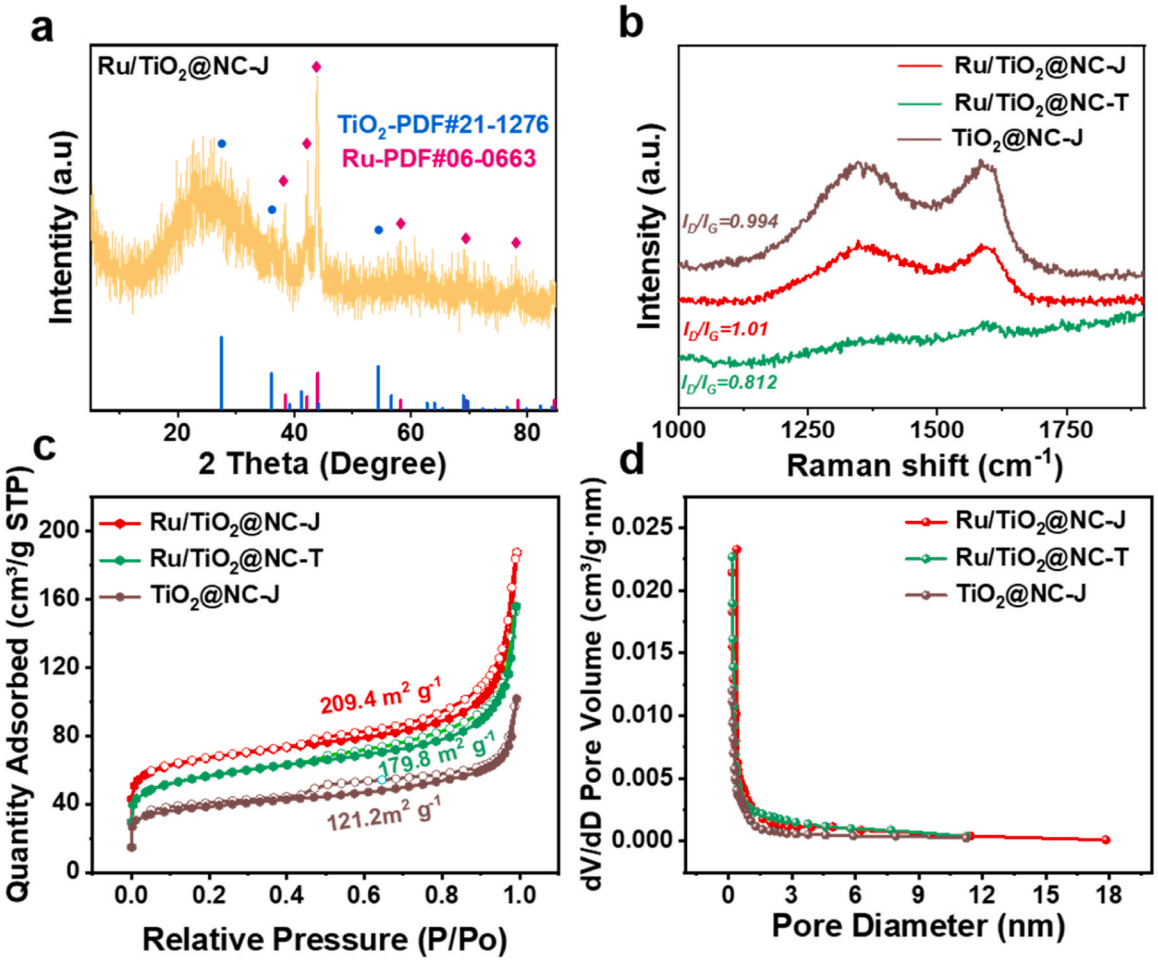

Fig. 3. (a) The XRD image of Ru/TiO_2 @NC-J. (b) Raman spectrum of Ru/TiO_2 @NC-J, Ru/TiO_2 @NC-T and TiO_2 @NC-J. (c) N_2 adsorption-desorption isotherm of Ru/TiO_2 @NC-J, Ru/TiO_2 @NC-T and TiO_2 @NC-J. (d) BJH pore size distribution of Ru/TiO_2 @NC-J, Ru/TiO_2 @NC-T and TiO_2 @NC-J.

species were basically in metallic form. To be more specific, the diffraction peak centered at 43.8°, belonged to the (110) facet of elemental Ru (PDF#06–0663). Rutile phase TiO_2 can also be observed, which was produced from the calcination of Ti-MOF. In Raman spectra (Fig. 3b) the peak centered at 1349 cm^{-1} regards to the D-band, which was typical in defective or disordered carbon materials, while the peak at 1590 cm^{-1} referred as G-band related to in-plane vibrations of graphitic structures [48]. Compared with the support (TiO_2 @NC-J) and the ordinary calcined sample (Ru/TiO_2 @NC-T), the D peak of Ru/TiO_2 @NC-J enhanced, leading to significant increased I_D/I_G value. These results showed the graphitization degree of carbon component increased and more defects produced during high temperature bombardment process, which could improve the stability of the catalyst and provide more potential active sites [49,50]. And high graphitized C has stronger π-π interaction, which was conducive to the rapid transfer of charge [51]. And the enhanced defective sites also helped modulate electronic structures and surface structures, to optimize the adsorption energies of intermediates during catalytic process [52].

In addition, the Brunauer-Emmett-Teller (BET) surface area and pore structure of the prepared Ru/TiO_2 @NC catalyst were calculated from N_2 adsorption-desorption isotherms in Fig. 3c. Notably, Ru/TiO_2 @NC-J maintains the highest BET specific surface area of 209.4 m^2g^{-1} and the largest pore volume of 0.21 cm^3g^{-1} among the pyrolysis products. Fig. 3d demonstrated the average pore size was 2–50 nm, testifying the mesoporous features of MOFs-derived materials. Thus, the large specific surface area and highly porous structure of the catalyst was warranted, which was more favorable for the exposure of active sites and the boost of mass transport. The detailed comparisons on the specific surface area, pore size, and pore volume of all the samples have been listed in Table S1.

As for the X-ray photoelectron spectroscopy (XPS) test, the full survey spectrum in Fig. S5 demonstrated the presence of Ru, Ti, O, N and C elements, which further testified the successful synthesis of Ru/TiO_2 @NC-J. In the high-resolution N 1 s XPS spectra (Fig. 4a), the peaks located at 403.7 and 400.8 eV were attributed to the oxidized and graphitic N, respectively. While the peaks at 398.2 and 396.3 eV were assigned to the interstitial N and substitutional N (i.e. Ti-N bond) in the TiO_2 lattice, respectively [53]. Detailed comparison of the relative content of N have been listed in Table S2. Two peaks corresponding to Ru^0 ($3d_{5/2}$) and Ru^0 ($3d_{3/2}$) at 280.6 eV and 284.7 eV indicated the formation of metallic Ru in the sample (Fig. 4b) [54]. While peaks located at 281.7 eV and 285.8 eV indicated the presence of RuO_2 because of the inevitable surface oxidation [27,55,56].

As seen in Fig. 4c, Ti^{4+} had binding energies of 464.3 and 458.6 eV attributed to Ti $2p_{1/2}$ and Ti $2p_{3/2}$, respectively. The peak of about 462.3 eV between Ti $2p_{3/2}$ and Ti $2p_{1/2}$ in Fig. 4c was the contribution of Ru $3p_{3/2}$ because of the partial overlap [57,58]. As the Ti^{4+} peaks shifted toward higher binding energies, indicating that charge transfer occurred between the metals Ru and TiO_2, leading to the reinforcement of the SMSI between the Ru and support. Meantime, the binding energies of O 1 s redshifted slightly (Fig. 4d), which was because of more oxygen vacancies (O_v) in TiO_2. Moreover, the intensity of EPR signals (Fig. S6) at g = 2.003 related respectively to O_v proved the point above. These O_v defects increased electron conductivity and leaded to a better intrinsic

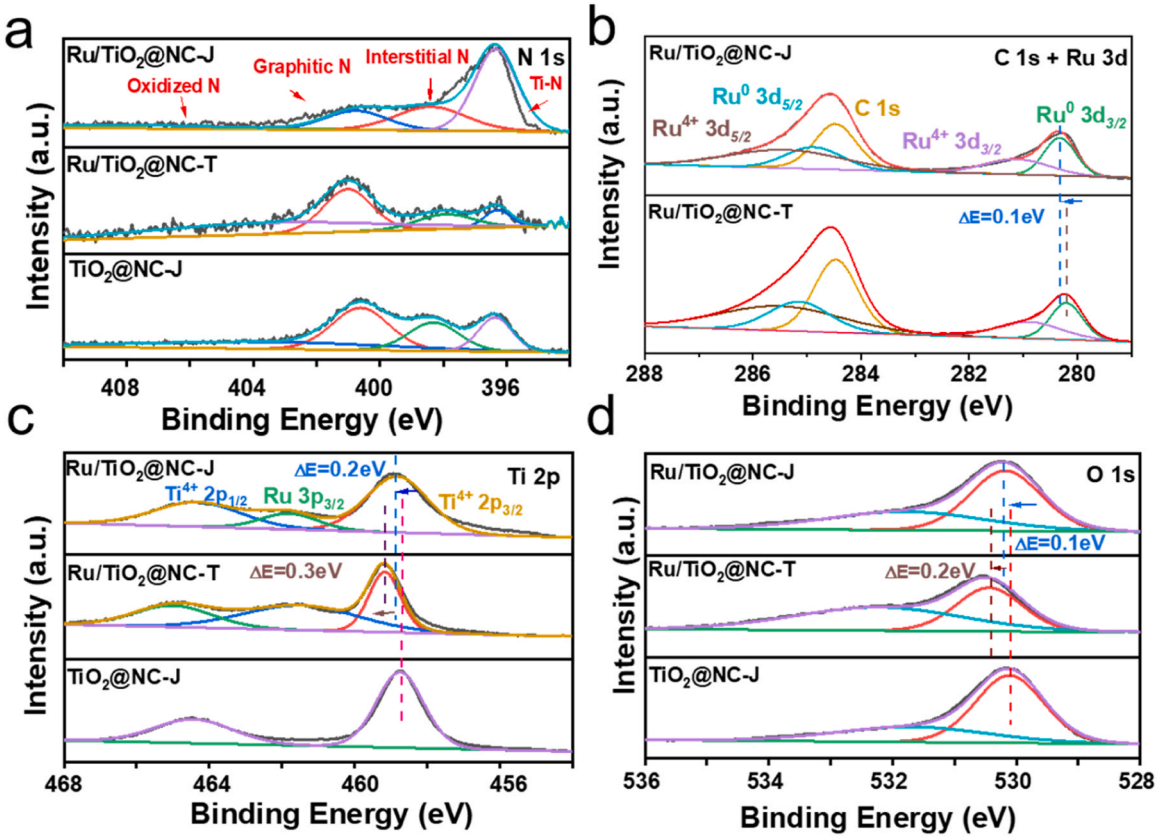

Fig. 4. High-resolution XPS spectra of (a) N 1 s, (b) Ru 3d and C 1 s, (c) Ti 2p, and (d) O 1 s of Ru/TiO_2 @NC-J , Ru/TiO_2 @NC-T and TiO_2 @NC-J.

HER activity [59]. As the binding energy shifts indicated charge rearrangement, the MOF derived porous support modulated the electronic configuration of the metallic Ru species, which promoted the charge transfer between Ru and TiO_2. Interestingly, due to the different calcination methods, the binding energies of Ru 3d of the Ru/TiO_2 @NC-J was 0.1 eV larger than that of Ru/TiO_2 @NC-T, which strengthen the adsorption of oxygen atoms and weaken the O-H bond in water molecules, thus improving the electrocatalysis performance.

As for the C 1 s high-resolution XPS spectra (Fig. S7), the peaks centered at 284.7 eV, 285.7 eV, 286.8 eV, and 289.0 eV were assigned to C-C, C-N, C═O, and C-C═O bonds, respectively [59,60]. Other detailed comparisons of different C contents have also been listed in Table S3. The results suggested that the high temperature shock synthesis contributed to the graphitization within pyrolysis process, and increased the N doping in the carbon matrix.

3.2. Electrocatalytic HER test of Ru/TiO_2 @NC-J

We carried out a series of experiments of pyrolysis temperature and time on electrocatalysts and HER performance. Firstly, we compared the performances of the catalysts with different pyrolysis times. 0.5 s is the minimum time for the heating equipment. Ru^{3+}/Ti-MOF were calcined at 0.5 s, 1 s and 1.5 s respectively at 1500 ℃, and the obtained samples were named as Ru/TiO_2 @NC-J-1500 ℃− 0.5 s, Ru/TiO_2 @NC-J-1500 ℃− 1 s and Ru/TiO_2 @NC-J-1500 ℃− 1.5 s, respectively. As shown in Fig. S8, the size of Ru nanoparticle of Ru/TiO_2 @NC-J-1500 ℃− 0.5 s, Ru/TiO_2 @NC-J-1500 ℃− 1 s and Ru/TiO_2 @NC-J-1500 ℃− 1.5 s are respectively 3.5 nm, 4.4 nm and 5.0 nm. Long calcination time leads to the growth of metal nanoparticles. Larger nanoparticle size may decrease the number of active sites and the active surface area [61]. As shown in Fig. S9, the overpotentials at a current density of 10 mA cm^{-2} are 11 mV, 17 mV and 29 mV for Ru/TiO_2 @NC-J-1500 ℃− 0.5 s, Ru/TiO_2 @NC-J-1500 ℃− 1 s and Ru/TiO_2 @NC-J-1500 ℃− 1.5 s, respectively. So, Ru/TiO_2 @NC-J-1500 ℃− 0.5 s has the best catalytic performance. We believe that the Joule heating is a very powerful method that can complete the transformation of MOF precursor in 0.5 s. We also compared the performance of catalysts with different pyrolysis temperature in different pH solutions. The Ru^{3+}/Ti-MOF were calcined at 1000 ℃, 1300 ℃, 1500 ℃, 1700 ℃ and 2000 ℃, and the obtained samples were named as Ru/TiO_2 @NC-J-1000 ℃, Ru/TiO_2 @NC-J-1300 ℃, Ru/TiO_2 @NC-J-1500 ℃, Ru/TiO_2 @NC-J-1700 ℃ and Ru/TiO_2 @NC-J-2000 ℃, respectively. TEM images of the catalysts Ru/TiO_2 @NC-J-1000 °C, Ru/TiO_2 @NC-J-1300 ℃, Ru/TiO_2 @NC-J-1500 ℃, Ru/TiO_2 @NC-J-1700 ℃ and Ru/TiO_2 @NC-J-2000 ℃ were shown in Fig. S10. It can be observed that the metal particles obtained by calcination at 1500 °C have the smallest size and the most uniform distribution. As shown in Fig. S11, the overpotentials at a current density of 10 mA cm^{-2} are 30 mV, 17 mV, 11 mV, 24 mV and 33 mV for Ru/TiO_2 @NC-J-1000 ℃, Ru/TiO_2 @NC-J-1300 ℃, Ru/TiO_2 @NC-J-1500 ℃, Ru/TiO_2 @NC-J-1700 ℃ and Ru/TiO_2 @NC-J-2000 ℃ in 1.0 M KOH solution, respectively. It can be seen that Ru/TiO_2 @NC-J-1500 ℃ has the best performance of HER in 1.0 M KOH solution. According to the above discussion, we chose the calcination method at 1500 °C for 0.5 s

The electrochemical HER catalytic activities of Ru/TiO_2 @NC-J, Ru/TiO_2 @NC-T and TiO_2 @NC-J and commercial Pt/C (20 wt%) were compared. As shown in Fig. 5a, among all a-prepared catalysts tested, Ru/TiO_2 @NC-J showed the best electrocatalytic activity in 1.0 M KOH media. It required an overpotential of 11 mV to drive 10 mA cm^{-2} current, only about half of that of Ru/TiO_2 @NC-T (Fig. S12a). Obviously, compared with the ordinary calcining method in tube furnace, the Ru/TiO_2 @NC-J prepared by Joule high temperature rapid bombardment showed higher efficiency, which may result from higher degree of graphitization and smaller Ru particle size. As shown in Fig. 5b, Ru/TiO_2 @NC-J had an amazing TOF of 8.6 s^{-1} at 50 mV, which was 3.3 times than that of Pt/C (2.6 s^{-1}). And at an overpotential of 100 mV, the TOF

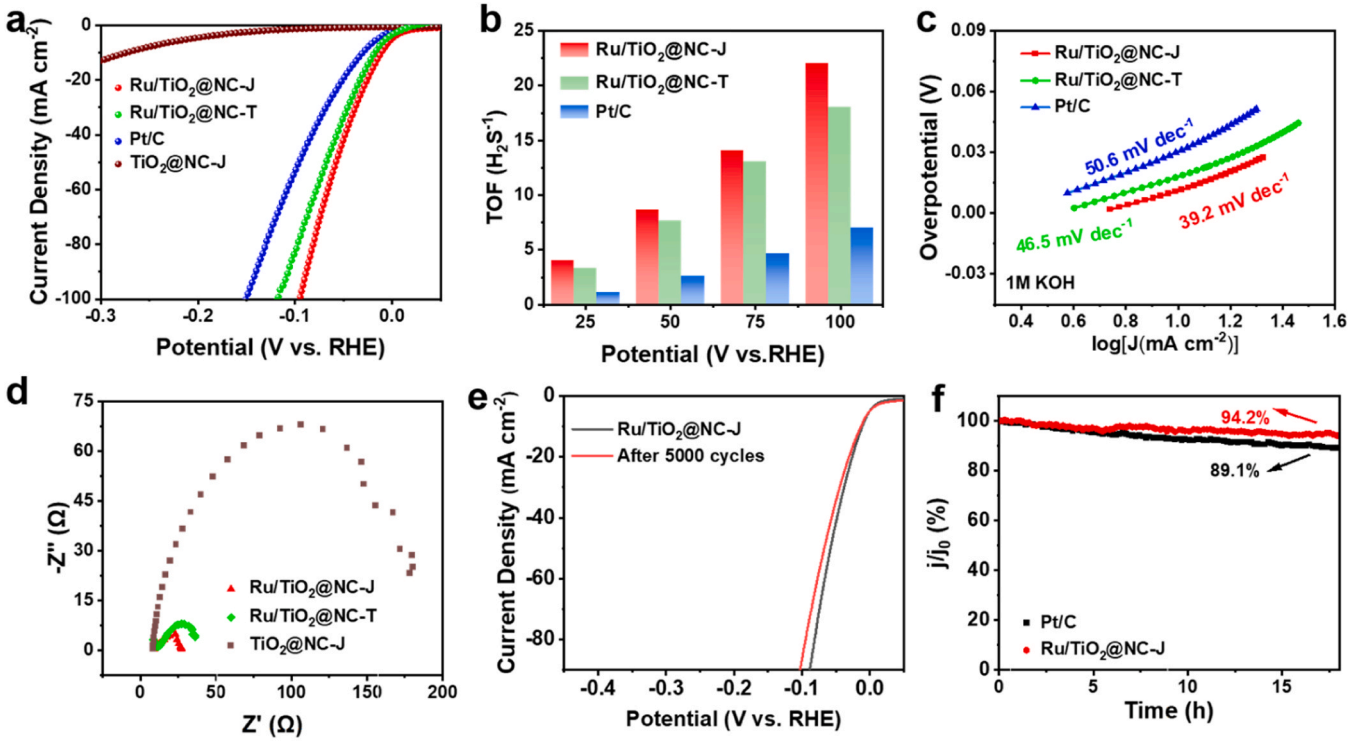

Fig. 5. HER performance in 1.0 M KOH. (a) HER polarization curves of Ru/TiO_2 @NC-J, Ru/TiO_2 @NC-T and TiO_2 @NC-J and Pt/C catalysts. (b) The TOF curves of catalyst at different overpotentials. (c) Tafel plots and (d) Nyquist plots of the Ru/TiO_2 @NC-J, Ru/TiO_2 @NC-T and TiO_2 @NC-J. (e) Polarization curves for Ru/TiO_2 @NC-J before and after 5000 cycles. (f) i-t curves of Ru/TiO_2 @NC-J and Pt/C.

of Ru/TiO_2 @NC-J reached 22.0 s^{-1}, which was also 3.14 times of Pt/C (7.0 s^{-1}). The Tafel slopes of Ru/TiO_2 @NC-J is 39.2 mV dec^{-1}, much lower than Pt/C (50.6 mV dec^{-1}) and Ru/TiO_2 @NC-T (46.5 mV dec^{-1}), which implied faster reaction kinetics (Fig. 5c). According to the Tafel slopes, HER follows the Volmer–Heyrovsky pathway in alkaline electrolytes. Ru has similar electron configuration like Pt. Ru possesses low water dissociation energy barrier, leading to better water dissociation ability [62]. At the same time, Ru shows a strong oxidizing ability due to its wide range of electron-rich characteristics near the Fermi level. This electronic environment provides an effective electron transfer path from the carrier to the Ru nanoparticle. It is beneficial to weaken the adsorption strength of H* and accelerate the release of H_2, thereby obtaining an effective HER [63]. Next, by extrapolating the Tafel curve the exchange current density (J_0) of the catalyst was obtained, which also indicated the intrinsic kinetics of the charge transfer reaction. In Fig. S12b, the J_0 of Ru/TiO_2 @NC-J reached 3.16 mA cm^{-2}, which was nearly twice of that of Pt/C (1.77 mA cm^{-2}). Obviously, Ru/TiO_2 @NC-J had a faster intrinsic HER kinetics.

To further prove the excellent performance of the Ru/TiO_2 @NC-J catalyst, we compared it with the catalyst reported in recent years (Table S4). It can be seen that the as-prepared catalyst counted as one of the best HER catalysts to date. Moreover, the double-layer capacitance (C_{dl}) was calculated via a test of CV curves at different sweep rates. In Fig. S13, the C_{dl} of the Ru/TiO_2 @NC-J almost double that of Pt/C, suggesting larger Electrochemical Active Surface Area (ECSA). Furthermore, electrochemical impedance spectroscopy (EIS) was applied to evaluate the electron transfer kinetics of the catalyst during the electrocatalysis. As expected, Ru/TiO_2 @NC-J had the smallest interface contact resistance (R_{ct}) (Fig. 5d). We attributed the reduced R_{ct} to the loading of Ru as well as the SMSI interaction, which synergistically increase the interface electron transfer kinetics.

At the same time, we also tested the stability of the as-developed catalyst. After 5000 CV cycles in 1.0 M KOH solution, the catalytic activity loss of Ru/TiO_2 @NC-J was neglectable (Fig. 5e). And the change of Ru/TiO_2 @NC-J at the current density of 10 mA cm^{-2} was small within 18 h, which is significantly better than that of commercially available Pt/C (Fig. 5f). In particular, the catalyst was able to achieve a higher current density at the same overpotential and outperformed commercial Pt/C (Fig. S14), which showed great promises for large-scale industrial hydrogen production.

In order to evaluate the catalyst in other working conditions, the HER activity of Ru/TiO_2 @NC-J in neutral (1.0 M PBS) and acidic (0.5 M H_2SO_4) media were also tested. For comparison, the HER performance of Ru/TiO_2 @NC-J, Ru/TiO_2 @NC-T, TiO_2 @NC-J, and Pt/C catalysts were also tested using the same method. As shown in Fig. 6a, the performance of catalyst Ru/TiO_2 @NC-J was much better than that of Ru/TiO_2 @NC-T, further testifying the superiority of this preparation method. The overpotential reached 69 mV at the current density of 10 mA cm^{-2} in 1.0 M PBS. According to Tafel slope curve (Fig. 6b), Ru/TiO_2 @NC-J has a lower slope (75.2 mV dec^{-1}) and a higher reaction and electron transfer kinetic. According to the Tafel slopes, HER follows the Volmer–Heyrovsky pathway in neutral electrolyte. In neutral electrolyte, the Ru/TiO_2 @NC-J has high adsorption strength towards the H_2O molecules. And this can boost the water dissociation into H^+ and OH^-. The dissociated H^+ is reduced into H* and eventually produce H_2 [59]. After repeat (5000 CV cycles) or long term (10 h) test in 1.0 M PBS solution, the catalytic activity loss of Ru/TiO_2 @NC-J was also neglectable (Fig. 6c). Its stability was even significantly better than that of Pt/C. In 0.5 M H_2SO_4, the overpotential reached 49 mV at the current density of 10 mA cm^{-2} (Fig. 6d). The Tafel slope is 52.3 mV dec^{-1}, which is also smaller than that of Ru/TiO_2 @NC-T (Fig. 6e). Volmer–Tafel pathway is the HER mechanism in acidic electrolytes [59]. In acidic electrolyte, Ru sites with rich electron favour the H^+ capturing in acidic solution and the reduction to H* . Then H* combines with adjacent H* on the cathode surface to produce H_2 [64]. And Ru/TiO_2 @NC-J also has good stability in an acidic medium (Fig. 6f).

Ru/TiO_2 @NC-J was also reevaluated by SEM, TEM images, XRD pattern and Raman spectrum (Fig. S15, S16) after stability test in

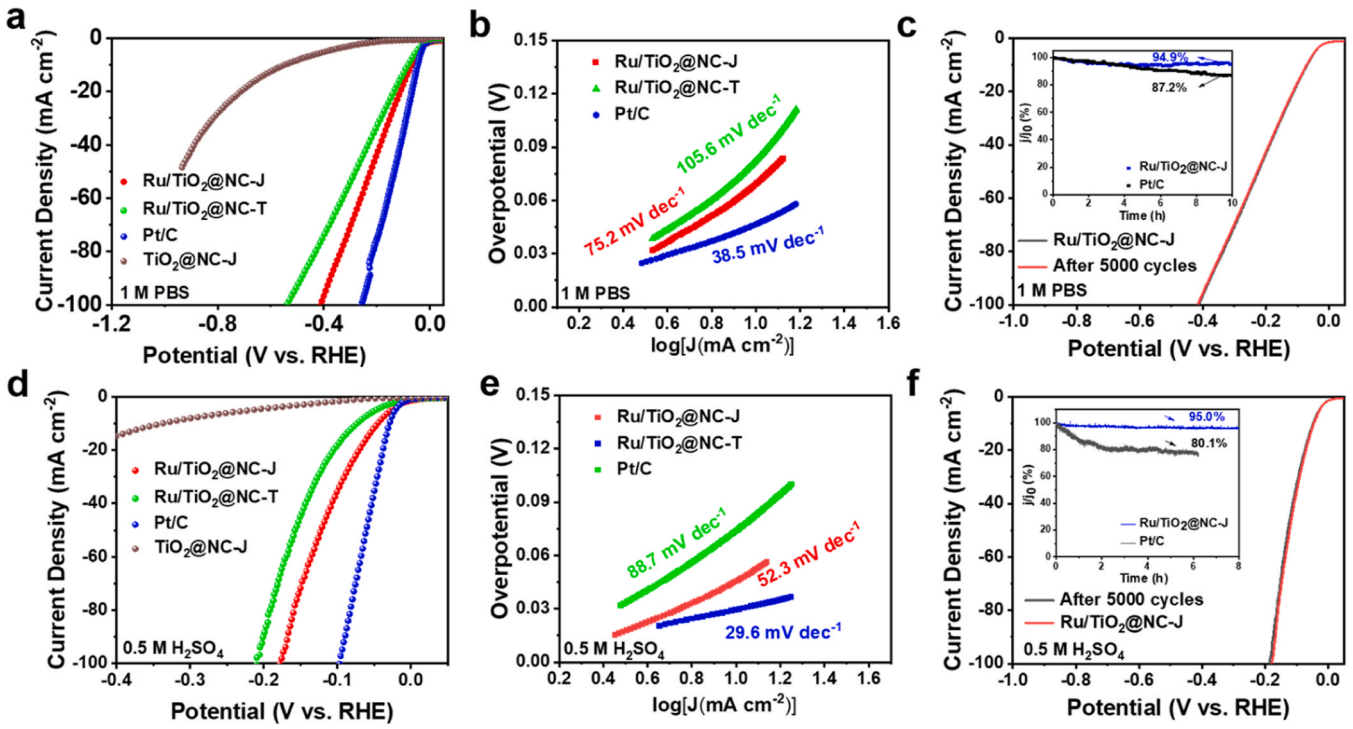

Fig. 6. HER polarization curves of Ru/TiO_2 @NC-J, Ru/TiO_2 @NC-T, Pt/C, and TiO_2 @NC-J in (a) 1.0 M PBS and (d) 0.5 M H_2SO_4. Corresponding Tafel plots in (b) 1.0 M PBS and (e) 0.5 M H_2SO_4. i-t curves of Ru/TiO_2 @NC-J for 10 h in (c) 1.0 M PBS and (f) 0.5 M H_2SO_4.

different electrolytes. No obvious changes can be observed, which suggested the excellent preservation of the composition and structure of Ru/TiO_2 @NC-J during the long-term HER process. Furthermore, in order to prove the electronic state before and after HER, XPS were performed. As exposed in Fig. S17, S18 and S19, the binding energy of Ru^0 3d exhibits red shift and Ti 2p displays blue shift after the stability test in 1.0 M KOH, 0.5 M H_2SO_4 and 1 M PBS solution. It indicated that electron transfer occurred between metal and carrier during the reaction, resulting in SMSI effect and slight change of electron cloud density. Note that only a slight shift occurred after chronopotentiometry test, further proving the excellent stability of Ru/TiO_2 @NC-J.

4. Conclusions

In conclusion, superfine Ru nanoparticles anchored on TiO_2 @nitrogen-doped carbon composite Ru/TiO_2 @NC-J has been developed by a super-fast high-temperature shock method for electrocatalytic HER performance. The TiO_2 @NC support function as hydrolysis dissociation and rapid electron transfer. Moreover, the superfine Ru nanoparticles can efficiently promote the adsorption/desorption of H intermediate. Such unique Ru/TiO_2 @NC-J results in prominent electrocatalytic HER performance in universal pH range. Especially in 1.0 M KOH solution, the overpotential was as low as 11 mV at the current density is 10 mA cm^{-2}, which was much better than the 20 wt% Pt /C and most of the state-of-art catalysts reported so far. The SMSI between Ru and support is active for the excellent stability. This work is the first case of superfine Ru nanoparticles anchored on TiO_2 @nitrogen-doped carbon as a pH-universal HER electrocatalyst via high-temperature shock method, which may drive the mass production of efficiently low-cost catalyst.

CRediT authorship contribution statement

Jinxiu Cai: Investigation, Writing – original draft. **Lingbo Zong:** Writing – review & editing, Supervision, Funding acquisition. **Kaicai Fan:** Formal analysis. **Fuxiang Song:** Data curation. **Zuming Wang:** Writing – review & editing. **Lei Wang:** Funding acquisition.

Declaration of Competing Interest

The authors declare that they have no known competing financial interests or personal relationships that could have appeared to influence the work reported in this paper.

Data availability

Data will be made available on request.

Acknowledgements

This work was financially supported by the National Natural Science Foundation of China, (Grant No. 52172208), Shandong Excellent Young Scientists Fund Program (Overseas, 2023HWYQ-091) and the Beijing Natural Science Foundation (No. 2232068).

Appendix A. Supporting information

Supplementary data associated with this article can be found in the online version at doi:10.1016/j.jallcom.2023.172279.

References

[1] L. Cai, B. Yan, H. Shi, P. Liu, G. Yang, A Medium-entropy oxide as a promising cocatalyst to promote photocatalytic hydrogen evolution, J. Colloid Interface Sci. 646 (2023) 625–632.
[2] L. Ji, Y. Wei, P. Wu, M. Xu, T. Wang, S. Wang, Q. Liang, T.J. Meyer, Z. Chen, Heterointerface engineering of Ni2P–Co2P nanoframes for efficient water splitting, Chem. Mater. 33 (2021) 9165–9173.
[3] L. Zong, K. Fan, P. Li, F. Lu, B. Li, L. Wang, Promoting oxygen reduction reaction on atomically dispersed Fe sites via establishing hydrogen bonding with the neighboring P atoms, Adv. Energy Mater. 13 (2022), 2203611.
[4] Y.Q. He, F. Yan, X. Zhang, C.L. Zhu, Y.Y. Zhao, B. Geng, S.L. Chou, Y. Xie, Y. J. Chen, Creating dual active sites in conductive metal-organic frameworks for efficient water splitting, Adv. Energy Mater. 13 (2023), 2204177.

[5] B. Jiang, Z. Wang, L. Cheng, Z. Chen, Y. Dong, X. Wang, T. Wang, X. Mao, Y. Gao, Z. Xu, K. Yin, K. Wu, Regulating charge distribution of Ru atoms in ruthenium phosphide/carbon nitride/carbon for promoting hydrogen evolution reaction, J. Alloy. Compd. 939 (2023), 168717.

[6] G.R. Xu, X. Jiang, T.T. Sun, X.L. Wang, B. Li, Z.X. Wu, H.Y. Liu, L. Wang, Ru branched nanostructure on porous carbon nanosheet for superior hydrogen evolution over a wide pH range, J. Alloy. Compd. 947 (2023), 169393.

[7] Y. Wei, G. Xu, Y. Wei, L. Ji, T. Wang, Z. Liu, S. Wang, Temperature-controlled synthesis of heterostructured Ru-Ru2P nanoparticles embedded in carbon nanofibers for highly efficient hydrogen production, Sci. China Mater. 65 (2022) 2675–2684.

[8] X. Li, D. Luo, F. Jiang, K. Zhang, S. Wang, S. Li, Q. Zha, Y. Huang, Y. Ni, Electronic modulation of metal-organic frameworks caused by atomically dispersed Ru for efficient hydrogen evolution, Small 19 (2023), 2301850.

[9] Y. Li, X. Zhang, L. Liu, H. Sheng, C. Li, L. Cao, H. Li, C. Xia, B. Dong, Ultra-low Pt doping and Pt-Ni pair sites in amorphous/crystalline interfacial electrocatalyst enable efficient alkaline hydrogen evolution, Small 19 (2023), 2300368.

[10] Y. Zhang, J. Yang, Z. Yu, Y. Hou, R. Jiang, J. Huang, F. Yang, S. Yao, L. Gao, W. Tang, Modulating carbon-supported transition metal oxide by electron-giving and electron-absorbing functional groups towards efficient overall water splitting, Chem. Eng. J. 416 (2021), 129124.

[11] J. He, F. Liu, Y. Chen, X. Liu, X. Zhang, L. Zhao, B. Chang, J. Wang, H. Liu, W. Zhou, Cathode electrochemically reconstructed V-doped CoO nanosheets for enhanced alkaline hydrogen evolution reaction, Chem. Eng. J. 432 (2022), 134331.

[12] X. Chen, Z. Wang, Y. Wei, X. Zhang, Q. Zhang, L. Gu, L. Zhang, N. Yang, R. Yu, High phase-purity 1T-MoS_2 ultrathin nanosheets by a spatially confined template, Angew. Chem. Int. Ed. 58 (2019) 17621–17624.

[13] B.W. Ren, D.Q. Li, Q.Y. Jin, H. Cui, C.X. Wang, A self-supported porous WN nanowire array: an efficient 3D electrocatalyst for the hydrogen evolution reaction, J. Mater. Chem. A 5 (2017) 19072–19078.

[14] H.Y. Jin, H. Zhang, J.Y. Chen, S.J. Mao, Z. Jiang, Y. Wang, A general synthetic approach for hexagonal phase tungsten nitride composites and their application in the hydrogen evolution reaction, J. Mater. Chem. A 6 (2018) 10967–10975.

[15] J. Li, Y. Zhang, W.J. Wei, G.C. Fan, Z.M. Wang, L.B. Zong, L. Wang, Dopamine-coated layered $Co_{0.85}Se$ as an efficient bifunctional oxygen electrocatalyst, New J. Chem. 47 (2023) 6287–6293.

[16] S. Liu, Y. Jiang, M. Yang, M. Zhang, Q. Guo, W. Shen, R. He, M. Li, Highly conductive and metallic cobalt-nickel selenide nanorods supported on Ni foam as an efficient electrocatalyst for alkaline water splitting, Nanoscale 11 (2019) 7959–7966.

[17] Y. Wei, Q. Tian, L. Ji, T. Wang, S. Wang, Phytic acid-assisted fabrication of porous leaf-like hollow structured Co2P @ C for efficient hydrogen evolution, J. Alloy. Compd. 934 (2023), 167924.

[18] X.H. Ji, X.Y. Chen, L.J. Zhang, C. Meng, Y.L. He, X. Zhang, Z.M. Wang, R.B. Yu, Anchoring nitrogen-doped Co_2P nanoflakes on $NiCo_2O_4$ nanorod arrays over nickel foam as high-performance 3D electrode for alkaline hydrogen evolution, Green. Energy Environ. 8 (2023) 470–477.

[19] W. He, L. Wang, H. Zhang, S. Gao, W. Yu, D. Yin, X. Dong, SnO_2@MoS_2 heterostructures grown on nickel foam as highly efficient bifunctional electrocatalyst for overall water splitting in alkaline media, J. Alloy. Compd. 938 (2023), 168678.

[20] A. Vijayan, N. Sandhyarani, Enhancing the catalytic activity of bulk MoS_2 towards hydrogen evolution reaction by the formation of MoS_2-MoO_3-Re_2O_7 heterostructure, J. Colloid Interface Sci. 623 (2022) 819–831.

[21] C. Meng, Z.M. Wang, L.J. Zhang, X.H. Ji, X.Y. Chen, R.B. Yu, Tuning the Mn dopant to boost the hydrogen evolution performance of CoP nanowire arrays, Inorg. Chem. 61 (2022) 9832–9839.

[22] Z.M. Wang, M. Cheng, R.B. Yu, Doping regulation in transition metal phosphides for hydrogen evolution catalysts, Chem. J. Chin. Univ. Chin. 43 (2022) 20.

[23] M. Qu, Y. Jiang, M. Yang, S. Liu, Q. Guo, W. Shen, M. Li, R. He, Regulating electron density of NiFe-P nanosheets electrocatalysts by a trifle of Ru for high-efficient overall water splitting, Appl. Catal. B Environ. 263 (2020), 118324.

[24] Y. Wang, B. Kong, D.Y. Zhao, H.T. Wang, C. Selomulya, Strategies for developing transition metal phosphides as heterogeneous electrocatalysts for water splitting, Nano Today 15 (2017) 26–55.

[25] Z. Zhang, P. Li, Q. Wang, Q. Feng, Y. Tao, J. Xu, C. Jiang, X. Lu, J. Fan, M. Gu, H. Li, H. Wang, Mo modulation effect on the hydrogen binding energy of hexagonal-close-packed Ru for hydrogen evolution, J. Mater. Chem. A 7 (2019) 2780–2786.

[26] J.S. Li, Y. Wang, C.H. Liu, S.L. Li, Y.G. Wang, L.Z. Dong, Z.H. Dai, Y.F. Li, Y.Q. Lan, Coupled molybdenum carbide and reduced graphene oxide electrocatalysts for efficient hydrogen evolution, Nat. Commun. 7 (2016) 11204.

[27] M. Yang, L. Jiao, H. Dong, L. Zhou, C. Teng, D. Yan, T.N. Ye, X. Chen, Y. Liu, H. L. Jiang, Conversion of bimetallic MOF to Ru-doped Cu electrocatalysts for efficient hydrogen evolution in alkaline media, Sci. Bull. 66 (2021) 257–264.

[28] S.M. Han, Q.B. Yun, S.Y. Tu, L.J. Zhu, W.B. Cao, Q.P. Lu, Metallic ruthenium-based nanomaterials for electrocatalytic and photocatalytic hydrogen evolution, J. Mater. Chem. A 7 (2019) 24691–24714.

[29] B. Qin, C. He, Y. Wei, L. Ji, T. Wang, Z. Chen, S. Wang, Interfacial engineering of heterostructured Mo2C-Ru nanoparticles dispersed on 3D interconnected carbon nanobelts for highly efficient hydrogen evolution, Electrochim. Acta 444 (2023), 141977.

[30] G.Z. Li, T. Sun, H.J. Niu, Y. Yan, T. Liu, S.S. Jiang, Q.L. Yang, W. Zhou, L. Guo, Triple interface optimization of Ru-based electrocatalyst with enhanced activity and stability for hydrogen evolution reaction, Adv. Funct. Mater. 33 (2023), 2212514.

[31] Y. Li, J. Abbott, Y. Sun, J. Sun, Y. Du, X. Han, G. Wu, P. Xu, Ru nanoassembly catalysts for hydrogen evolution and oxidation reactions in electrolytes at various pH values, Appl. Catal. B: Environ. 258 (2019), 117952.

[32] C. Li, S.H. Kim, H.Y. Lim, Q. Sun, Y. Jiang, H.-J. Noh, S.-J. Kim, J. Baek, S.K. Kwak, J.-B. Baek, Self-accommodation induced electronic metal-support interaction on ruthenium site for alkaline hydrogen evolution reaction, Adv. Mater. 35 (2023), 2301369.

[33] J. Mahmood, F. Li, S.M. Jung, M.S. Okyay, I. Ahmad, S.J. Kim, N. Park, H.Y. Jeong, J.B. Baek, An efficient and pH-universal ruthenium-based catalyst for the hydrogen evolution reaction, Nat. Nanotechnol. 12 (2017) 441–446.

[34] R. Luo, Z. Li, R. Li, C. Jiang, R. Qi, M. Liu, H. Lin, R. Huang, C. Luo, H. Peng, Ultrafine Ru nanoparticles derived from few-layered Ti3C2Tx MXene templated MOF for highly efficient alkaline hydrogen evolution, Int. J. Hydrog. Energy 47 (2022) 32787–32795.

[35] X. Kong, K. Xu, C. Zhang, J. Dai, S. Norooz Oliaee, L. Li, X. Zeng, C. Wu, Z. Peng, Free-standing two-dimensional Ru nanosheets with high activity toward water splitting, ACS Catal. 6 (2016) 1487–1492.

[36] Y. Pi, Z. Qiu, Y. Sun, H. Ishii, Y.-F. Liao, X. Zhang, H.-Y. Chen, H. Pang, Synergistic mechanism of sub-nanometric Ru clusters anchored on tungsten oxide nanowires for high-efficient bifunctional hydrogen electrocatalysis, Adv. Sci. 10 (2023), 2206096.

[37] Z. Yin, J. Liang, Z. Zhang, H. Luo, J. Zhou, Construction of superhydrophilic metal-organic frameworks with hierarchical microstructure for efficient overall water splitting, J. Colloid Interface Sci. 623 (2022) 405–416.

[38] Y.L. He, L.J. Zhang, Y.Z. Wei, X. Zhang, Z.M. Wang, R.B. Yu, Semicrystalline $SrTiO_3$-decorated anatase Tio2 nanopie as heterostructure for efficient photocatalytic hydrogen evolution, Small Methods 6 (2022), 2101567.

[39] T. Qiu, Z. Liang, W. Guo, S. Gao, C. Qu, H. Tabassum, H. Zhang, B. Zhu, R. Zou, Y. Shao-Horn, Highly exposed ruthenium-based electrocatalysts from bimetallic metal-organic frameworks for overall water splitting, Nano Energy 58 (2019) 1–10.

[40] Z. Cui, T. Fan, L. Chen, R. Fang, C. Li, Y. Li, Encapsulation of ultrafine Pd nanoparticles within the shallow layers of UiO-67 for highly efficient hydrogenation reactions, Sci. China Chem. 64 (2020) 109–115.

[41] Y. Wang, C. Wang, H. Shang, M. Yuan, Z. Wu, J. Li, Y. Du, Self-driven Ru-modified NiFe MOF nanosheet as multifunctional electrocatalyst for boosting water and urea electrolysis, J. Colloid Interface Sci. 605 (2022) 779–789.

[42] Z.M. Wang, N.L. Yang, D. Wang, When hollow multishelled structures (HoMSs) meet metal-organic frameworks (MOFs), Chem. Sci. 11 (2020) 5359–5368.

[43] H.S. Jadhav, H.A. Bandal, S. Ramakrishna, H. Kim, Critical review, recent updates on zeolitic imidazolate framework-67 (ZIF-67) and its derivatives for electrochemical water splitting, Adv. Mater. 34 (2022), e2107072.

[44] S. Sanati, A. Morsali, H. Garcia, First-row transition metal-based materials derived from bimetallic metal-organic frameworks as highly efficient electrocatalysts for electrochemical water splitting, Energy Environ. Sci. 15 (2022) 3119–3151.

[45] J. Li, C. Wang, X. Chen, Y. Zhang, Y. Zhang, K. Fan, L. Zong, L. Wang, Flash synthesis of ultrafine and active NiRu alloy nanoparticles on N-rich carbon nanotubes via joule heating for efficient hydrogen and oxygen evolution reaction, J. Alloy. Compd. 959 (2023), 170571.

[46] S. Dou, J. Xu, X. Cui, W. Liu, Z. Zhang, Y. Deng, W. Hu, Y. Chen, High-temperature shock enabled nanomanufacturing for energy-related applications, Adv. Energy Mater. 10 (2020), 2001331.

[47] Y. He, X. Zhang, Y. Wei, X. Chen, Z. Wang, R. Yu, Ti-MOF derived N-doped TiO_2 nanostructure as visible-light-driven photocatalyst, Chem. Res. Chin. Univ. 36 (2020) 447–452.

[48] B. Yan, D. Liu, X. Feng, M. Shao, Y. Zhang, Ru species supported on MOF-derived N-doped TiO_2/C hybrids as efficient electrocatalytic/photocatalytic hydrogen evolution reaction catalysts, Adv. Funct. Mater. 30 (2020), 2003007.

[49] S. Dou, J. Xu, X. Cui, W. Liu, Z. Zhang, Y. Deng, W. Hu, Y. Chen, High-temperature shock enabled nanomanufacturing for energy-related applications, Adv. Energy Mater. 10 (2020), 2001331.

[50] S. Liu, Y. Shen, Y. Zhang, B. Cui, S. Xi, J. Zhang, L. Xu, S. Zhu, Y. Chen, Y. Deng, W. Hu, Extreme environmental thermal shock induced dislocation-rich pt nanoparticles boosting hydrogen evolution reaction, Adv. Mater. 34 (2022), e2106973.

[51] Y. Jiang, L. Yang, T. Sun, J. Zhao, Z. Lyu, O. Zhuo, X. Wang, Q. Wu, J. Ma, Z. Hu, Significant contribution of intrinsic carbon defects to oxygen reduction activity, ACS Catal. 5 (2015) 6707–6712.

[52] Y. Jia, L. Zhang, A. Du, G. Gao, J. Chen, X. Yan, C.L. Brown, X. Yao, Defect graphene as a trifunctional catalyst for electrochemical reactions, . Mater. 28 (2016) 9532–9538.

[53] J. Wang, D.N. Tafen, J.P. Lewis, Z. Hong, A. Manivannan, M. Zhi, M. Li, N. Wu, Origin of photocatalytic activity of nitrogen-doped TiO_2 nanobelts, J. Am. Chem. Soc. 131 (2009) 12290–12297.

[54] A. Salah, H.D. Ren, N. Al-Ansi, H. Tan, F. Yu, L. Yanchun, B.M. Thamer, A. Al-Salihy, L. Zhao, Y. Li, Dispersing small Ru nanoparticles into boron nitride remodified by reduced graphene oxide for high-efficient electrocatalytic hydrogen evolution reaction, J. Colloid Interface Sci. 644 (2023) 378–387.

[55] X. Cheng, H. Wang, M. Ming, W. Luo, Y. Wang, Y. Yang, Y. Zhang, D. Gao, J. Bi, G. Fan, Well-defined Ru nanoclusters anchored on carbon: facile synthesis and high electrochemical activity toward alkaline water splitting, ACS Sustain. Chem. Eng. 6 (2018) 11487–11492.

[56] J.Q. Chi, X.J. Zeng, X. Shang, B. Dong, Y.M. Chai, C.G. Liu, M. Marin, Y. Yin, Embedding RhPx in N, P Co-doped carbon nanoshells through synergetic phosphorization and pyrolysis for efficient hydrogen evolution, Adv. Funct. Mater. 29 (2019), 1901790.

[57] M. Sathiya, K. Ramesha, G. Rousse, D. Foix, D. Gonbeau, A.S. Prakash, M. L. Doublet, K. Hemalatha, J.M. Tarascon, High performance Li_2Ru_1-$yMnyO_3$ ($0.2 \leq y \leq 0.8$) cathode materials for rechargeable lithium-ion batteries: their understanding, Chem. Mater. 25 (2013) 1121–1131.
[58] S. Nong, W. Dong, J. Yin, B. Dong, Y. Lu, X. Yuan, X. Wang, K. Bu, M. Chen, S. Jiang, L.-M. Liu, M. Sui, F. Huang, Well-dispersed ruthenium in mesoporous crystal TiO_2 as an advanced electrocatalyst for hydrogen evolution reaction, J. Am. Chem. Soc. 140 (2018) 5719–5727.
[59] W. Xu, H. Xie, F. Cao, S. Ran, Y. Duan, B. Li, L. Wang, Enhanced interaction between Ru nanoparticles and N, C-modified mesoporous TiO_2 for efficient electrocatalytic hydrogen evolution at all pH values, J. Mater. Chem. A 10 (2022) 23751–23759.
[60] J. Wang, G. Liu, K. Fan, D. Zhao, B. Liu, J. Jiang, D. Qian, C. Yang, J. Li, N-doped carbon coated anatase TiO_2 nanoparticles as superior Na-ion battery anodes, J. Colloid Interface Sci. 517 (2018) 134–143.
[61] Z. Chen, J. Lu, Y. Ai, Y. Ji, T. Adschiri, L. Wan, Ruthenium/graphene-like layered carbon composite as an efficient hydrogen evolution reaction electrocatalyst, ACS Appl. Mater. Interfaces 8 (2016) 35132–35137.
[62] A. Salah, L. Zhang, H. Tan, F. Yu, Z. Lang, N. Al-Ansi, Y. Li, Advanced Ru/Ni/WC@NPC multi-interfacial electrocatalyst for efficient sustainable hydrogen and chlor-alkali Co-production, Adv. Energy Mater. 12 (2022), 2200332.
[63] Y. Sun, Z. Xue, Q. Liu, Y. Jia, Y. Li, K. Liu, Y. Lin, M. Liu, G. Li, C.-Y. Su, Modulating electronic structure of metal-organic frameworks by introducing atomically dispersed Ru for efficient hydrogen evolution, Nat. Commun. 12 (2021) 1369.
[64] X. Wang, C. Xu, M. Jaroniec, Y. Zheng, S.-Z. Qiao, Anomalous hydrogen evolution behavior in high-pH environment induced by locally generated hydronium ions, Nat. Commun. 10 (2019) 4876.